fluids

MDPI

Article

The Aerodynamic Effects of a 3D Streamlined Tail on the Windsor Body

Jeff Howell *, Max Varney, Martin Passmore and Daniel Butcher

Aeronautical and Automotive Engineering, Loughborough University, Loughborough LE11 3TU, UK
* Correspondence: j.p.howell@lboro.ac.uk

Abstract: The aerodynamic drag reduction of road vehicles is of continuing interest. The drag arising from the rear surfaces is usually the dominant component, but this can be alleviated by the tapering of the rear body. The effects on the aerodynamic characteristics of a simple body from adding an elongated tapered tail have been investigated in a wind tunnel experiment. The streamlined tail consists of a constant rear body side taper added to a constant upper body taper. The results have been compared with an earlier study of the same body with upper body tapering only. The effects of truncating the long tail are explored. Adding the planform tapering reduces the impact of the slant edge vortices, and drag and lift are substantially reduced. The lateral aerodynamic characteristics are largely unaffected.

Keywords: car aerodynamics; drag and lift; drag reduction; streamlined tail

check for updates

Citation: Howell, J.; Varney, M.; Passmore, M.; Butcher, D. The Aerodynamic Effects of a 3D Streamlined Tail on the Windsor Body. *Fluids* **2023**, *8*, 59. https://doi.org/10.3390/fluids8020059

Academic Editors: Mehrdad Massoudi and Pier Marzocca

Received: 15 December 2022
Revised: 26 January 2023
Accepted: 30 January 2023
Published: 8 February 2023

Copyright: © 2023 by the authors. Licensee MDPI, Basel, Switzerland. This article is an open access article distributed under the terms and conditions of the Creative Commons Attribution (CC BY) license (https://creativecommons.org/licenses/by/4.0/).

1. Introduction

The aerodynamic drag of cars continues to be reduced, albeit slowly, driven most recently by the need to improve the range of electric vehicles but also by the ongoing need to reduce emissions, particularly CO_2. For most of the recent past this drag reduction has been achieved by the fine tuning of vehicle shapes, within design constraints, and by attention to detail, but also through CO_2 tax incentives. The rise in popularity of electric vehicles provides additional opportunities. These include, for example, reduced cooling airflow and smoother underfloor architecture, but also a greater design freedom to enhance the perceived cutting edge technology, especially through streamlining.

It has been recognised from the earliest days of the practical automobile that high speed performance and fuel economy can be improved by reducing aerodynamic drag. It is now 100 years since Jaray developed low resistance car shapes in the Zeppelin wind tunnel based on airship principles (see Ludvigsen, [1]). In the 1920s and 1930s, the concept of streamlining took hold of the public imagination and was applied to all forms of transportation, including cars. Highly streamlined cars were, however, susceptible to crosswinds and could be impractical, but German car aerodynamicists, including Kamm and Koenig-Fachsenfeld, [2], found that cutting off the tail resulted in a negligible drag penalty. For a comprehensive review of the early history of car aerodynamics, the reader is referred to Ludvigsen, [1], Hucho, [3], or Schütz, [4], and Edgar, [5].

Howell et al. [6], have reviewed the available literature on truncating streamlined tails for various simple bodies and vehicle shapes. It was remarked how little data is available on the effects of streamlined tails on non-axisymmetric bodies whether representative of road vehicles or not. It was shown that truncating the tail of a streamlined shape resulted in an approximately linear increase in drag coefficient; a result which was supported by a CFD study of a streamlined tail on the Windsor Body created by a taper on the rear upper body. A subsequent wind tunnel investigation of this body, with and without wheels by Howell et al. [7], gave similar results but suggested that the increase in drag from truncation could also be given by the prediction of Hoerner, [8], that the drag increase is a function

of the base area to the power 1.5. The results also indicated that the study by Mair, [9], on axi-symmetric bodies, which has often been cited as confirmation that a highly truncated streamlined shape shows almost no drag increase over the streamlined form, was not repeated for any of the car-like shapes investigated.

The wind tunnel study reported in this paper considers the effect of combined planform and upper surface tapering, which is referred to as 3D tapering, on the aerodynamic characteristics of a simple body representing a passenger car. It complements and is compared to the investigation by Howell et al. [7], where rear body tapering was applied to the upper surface only, here called 2D tapering. The paper adds to the limited knowledge of the effects of extreme rear body shaping on the potential aerodynamic drag reduction of cars.

2. Experimental Set-Up

2.1. Model

The baseline model for this experiment is the Windsor Body in squareback configuration. The Windsor Body has been extensively tested over many years for various investigations into different aspects of road vehicle aerodynamics from ground simulation to bi-stability and including rear body drag reduction. The basic geometry crudely represents a quarter-scale medium sized hatchback. The squareback model length is 1.044 m and the width and height are 0.289 m and 0.389 m, respectively. The frontal area, A, is 0.1124 m^2.

The basic body is shown in Figure 1 with the extended tails of different lengths. The shape is overlaid on the Windsor body with a 2D tapered tail, shown in grey. Both tails have a flat floor. The main body is machined from high density foam, but each tail is a separate construction and is fabricated from a wood sheet; in part to keep the weight of the long tail lengths low. A good surface finish was achieved on the forebody and tails. The final very short section to complete the streamlined tail is made from light foam.

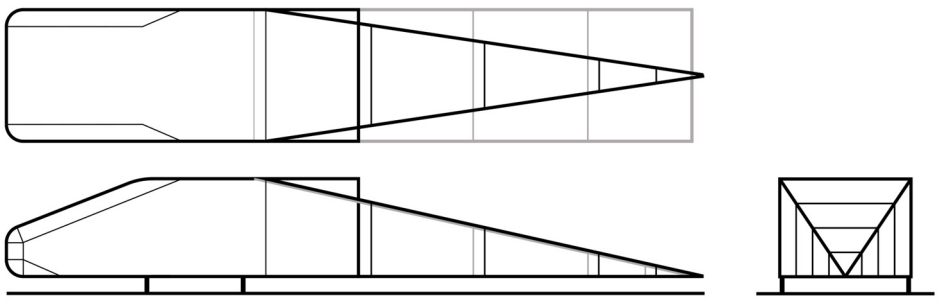


Figure 1. Windsor Body with streamlined tail in 2D and 3D configurations.

The rear upper surface taper angle is constant at 12.5°, as with the earlier study, [7], and both rear side taper angles are 8.3°. The tail length is denoted by L_T and is the horizontal projection of the slant surface length. An internal structural part of the base model meant that the mid-section of the body was extended by 0.030 m so that the leading edge of the tapering of the top and side surfaces was similarly moved aft in comparison with the 2D tapered body. The lengths of the tapered tails were the same for both 3D and 2D cases. The overall length of the initial tapered body, which has a tail length, L_T, of 0.310 m, is then 0.030 m longer than the overall length of the squareback model. Additional tail sections have lengths of 0.650 m, 0.990 m and 1.160 m, as with the 2D tapered tails. The final foam section is 0.14 m long and has a trailing edge thickness less than 0.001 m. The aspect ratio of the base surface, the width/height ratio, is the same for all truncated tails as well as the squareback case. The squareback configuration represents the body with $L_T = 0$. It is recognized that this is inconsistent with the other tails but introduces a very small drag increment from increased skin friction that is ignored. For all the tests reported here the ground clearance was set at 0.050 m.

2.2. Wind Tunnel

The wind tunnel used for this experiment was the Loughborough University Large Wind Tunnel. This tunnel is an open circuit, closed working section facility of novel design, as described by Johl, [10]. The test section is 1.92 m wide by 1.32 m high, with 0.2 m by 0.2 m corner fillets, and has a length of 3.6 m. The working section area, A_{WT}, is 2.45 m^2. The long working section ensured that the trailing edge for the longest body was well upstream of the start of the diffuser.

The operating airspeed range for the wind tunnel is 5–45 m/s. All of the data presented here was carried out at a nominal wind speed of 40 m/s unless stated otherwise. At 40 m/s the turbulence intensity is 0.2%. The working section floor represents the fixed ground surface. The boundary layer on the floor of the working section at the turntable centre in the empty tunnel has a total thickness (99% freestream velocity) of 0.060 m, and the displacement thickness is 0.009 m.

A 6-component virtual-centre balance is installed beneath the wind tunnel. The balance can be yawed and connects to a turntable flush with the wind tunnel floor. It is connected to the model via four 0.008 m diameter unshielded struts which pass through small diameter holes in the turntable. The struts are inset 0.010 m from the bodysides and are 0.286 m apart. The strut drag is included in the overall drag data. A schematic of the test set-up is shown in Figure 2.

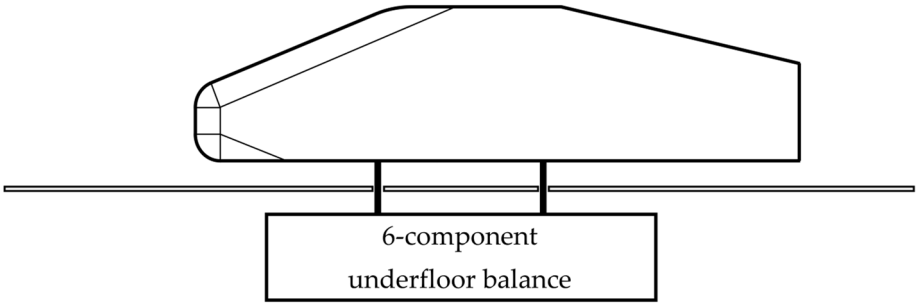


Figure 2. Schematic showing the Windsor body mounted above the wind tunnel floor.

Force coefficients are non-dimensionalized with respect to the frontal area, A, while moments are non-dimensionalized with respect to the frontal area and wheelbase, L_W. In the earlier study, [7], which included a body with wheels, the wheelbase, L_W, was 0.637 m and mid-wheelbase, which defines the moment centre, was 0.561 m aft of the model leading edge, (0.537 × squareback model length). These dimensions and the model mountings are retained for the current tests. The axis centre is at mid-wheelbase at ground level on the centre-line. Force, F, and moment, M, coefficients are corrected using the continuity method, such that:

$$(C_F, C_M)_c = (C_F, C_M)_m (1 - B)^2, \quad (1)$$

where c, m denote corrected and measured values, respectively, and B is the blockage ratio, A/A_{WT}. The blockage ratio for all the bodies tested here is 4.6%.

Although no pressure data was acquired for this paper, a reference to earlier pressure measurements is included. Pressure coefficients, C_P, are corrected using:

$$(1 - C_P)_c = (1 - C_P)_m (1 - B)^2. \quad (2)$$

The accuracy of the underfloor balance allows force and moment coefficients to be determined significantly better than 1 count, (0.001), at normal operating wind speeds for a model of Windsor body size. The overall repeatability for the drag coefficient is typically ±0.002.

The force and moment characteristics, obtained in the wind tunnel, for the bodies with different tail lengths over a range of yaw angles are presented in the following section.

3. Results

The basic longitudinal aerodynamic characteristics, lift and drag, are shown in Figure 3a,b. Each graph shows the coefficient as a function of yaw angle for the range of tail lengths. The graphs for each coefficient are plotted to the same scale to facilitate direct comparisons. Data was obtained for a yaw angle between ±15° at 5° intervals. The precise behaviour of the coefficients close to 0° yaw cannot be determined.

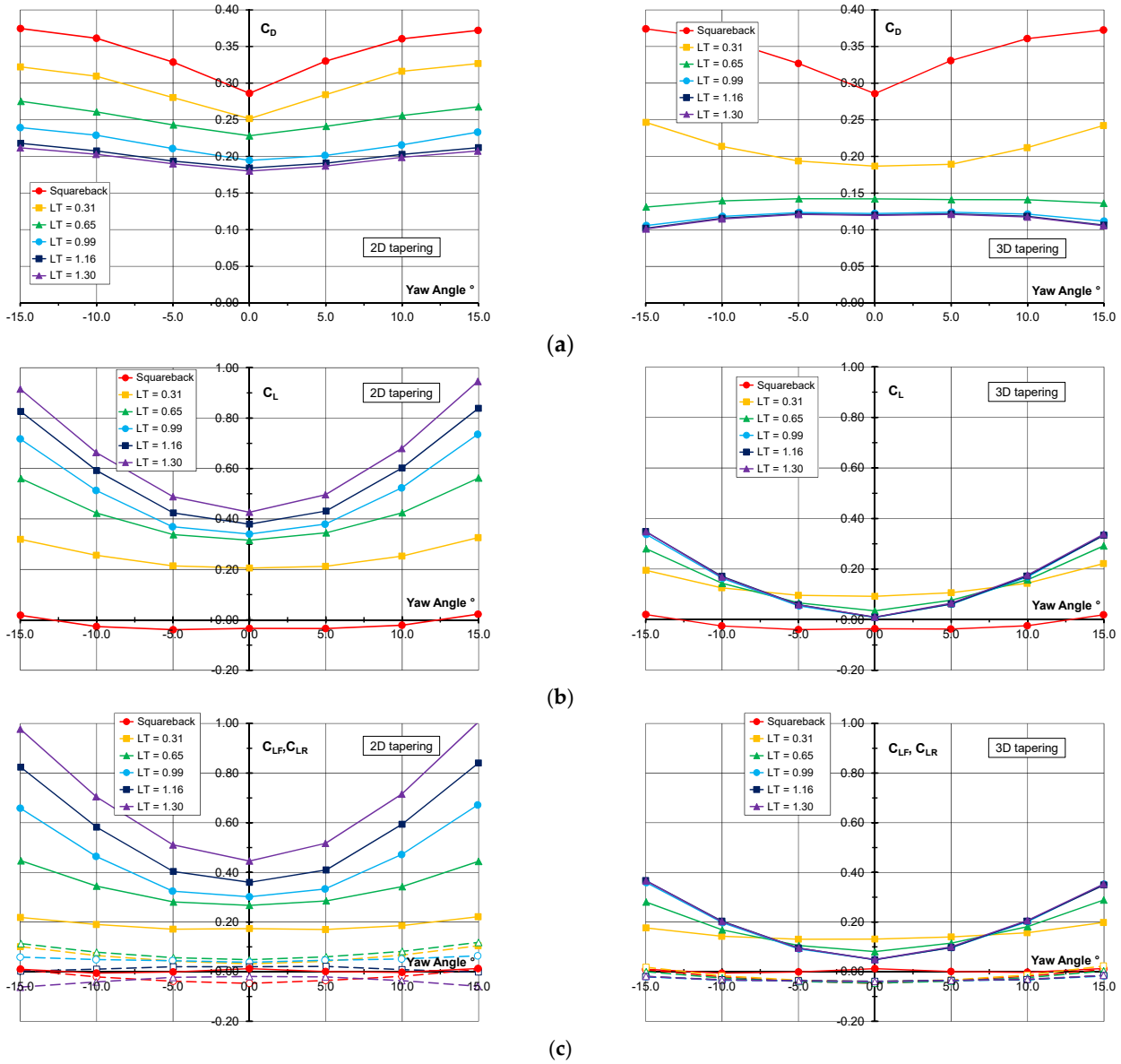


Figure 3. (**a**). Drag coefficient. (Left) 2D tapered body, (Right) 3D tapered body. (**b**). Lift coefficient. (Left) 2D tapered body, (Right) 3D tapered body. (**c**). Front/rear axle lift coefficients. (Left) 2D tapered body, (Right) 3D tapered body. Front, (open symbols, dashed lines), rear, (solid symbols and lines).

For the 2D tapered case, the drag coefficient at zero yaw and the drag rise with yaw angle reduce with increasing tail length. The drag rise with yaw reduces with increasing yaw angle. For the 3D tapered bodies the drag at 0° yaw shows a larger reduction than in the 2D case. The drag variation with yaw is approximately parabolic in form for all the 3D tapered tails. The drag increases with yaw for the shortest tail tested, but reduces with yaw for the longer tails.

The overall lift coefficient for the squareback body is close to zero and increases only slowly with the yaw angle. For the 2D tapered tails, the lift at 0° yaw and the increase of lift with yaw increase with increasing tail length. In the case of the 3D tapered body with the shortest tail tested, the lift increase at zero yaw is reduced in comparison with the 2D case, but the lift increase with yaw is comparable. For longer tails the zero yaw lift is reduced, but the lift increase with yaw increases again, although the rise is not as pronounced as in the 2D case, and becomes almost independent of yaw for tails longer than 0.65 m. The drag and lift coefficients as a function of tail length at zero yaw are summarised in the Discussion section.

The variation of the front and rear axle lift coefficients with yaw are shown in Figure 3c for the 2D and 3D tapered cases. The rear axle lift is shown by the solid symbols and line, while the front axle lift is given by the open symbols and dashed lines.

For both cases most of the lift variation is at the rear axle. For the 2D tapered case, both the rear axle lift at 0° yaw and the rear lift rise with yaw increases with taper length. For the shorter taper lengths the incremental lift is focused on the taper leading edge and acts upstream of the rear axle, producing a slightly increased front axle component. As the tail length increases, the incremental lift increasingly acts behind the rear axle and the front axle lift component reduces and its increase with yaw becomes negative. For the 3D tapered body, most of the lift variation is reflected in the rear axle lift, as shown in Figure 3c (right). The front axle lift coefficient is almost the same for the squareback and all of the tapered tail cases.

The effect of Reynolds number on the drag and lift coefficients at 0° yaw angle is shown in Figure 4. The range of Reynolds numbers represents wind tunnel airspeeds from approximately 10 m/s to 40 m/s. The solid symbols and lines show the drag coefficients, while the open symbols with dashed lines show the lift coefficients. The drag coefficients reduce very slightly with increasing Reynolds number, but the drag benefit from the elongated tail increases with the increasing Reynolds number. The lift coefficient is effectively constant for Reynolds numbers greater than 1.5×10^6.

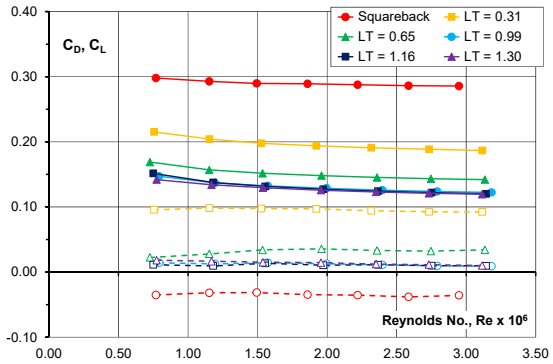


Figure 4. Effect of Reynolds number on drag and lift coefficients at 0° yaw. Drag coefficient, (solid symbols), lift coefficient, (open symbols).

The lateral aerodynamic characteristics, side force, yawing moment and rolling moment are presented in Figure 5a–c. The side force coefficient increase at yaw for the 3D tapered case is very similar to that for the 2D tapered bodies with the side force derivative, the change of side force with yawing moment, reducing with increasing tail length and becoming increasingly non-linear. The only noticeable change is for the shortest tapered 3D case, which shows a small reduction compared with the 2D body.

The yawing moment characteristics shown in Figure 5b are not significantly altered by introducing planform tapering. Only the intermediate length tails, L_T = 0.65 and 0.99, show a small increase in the yawing moment coefficient. The yawing moment derivative increases with tail length, as does the non-linearity.

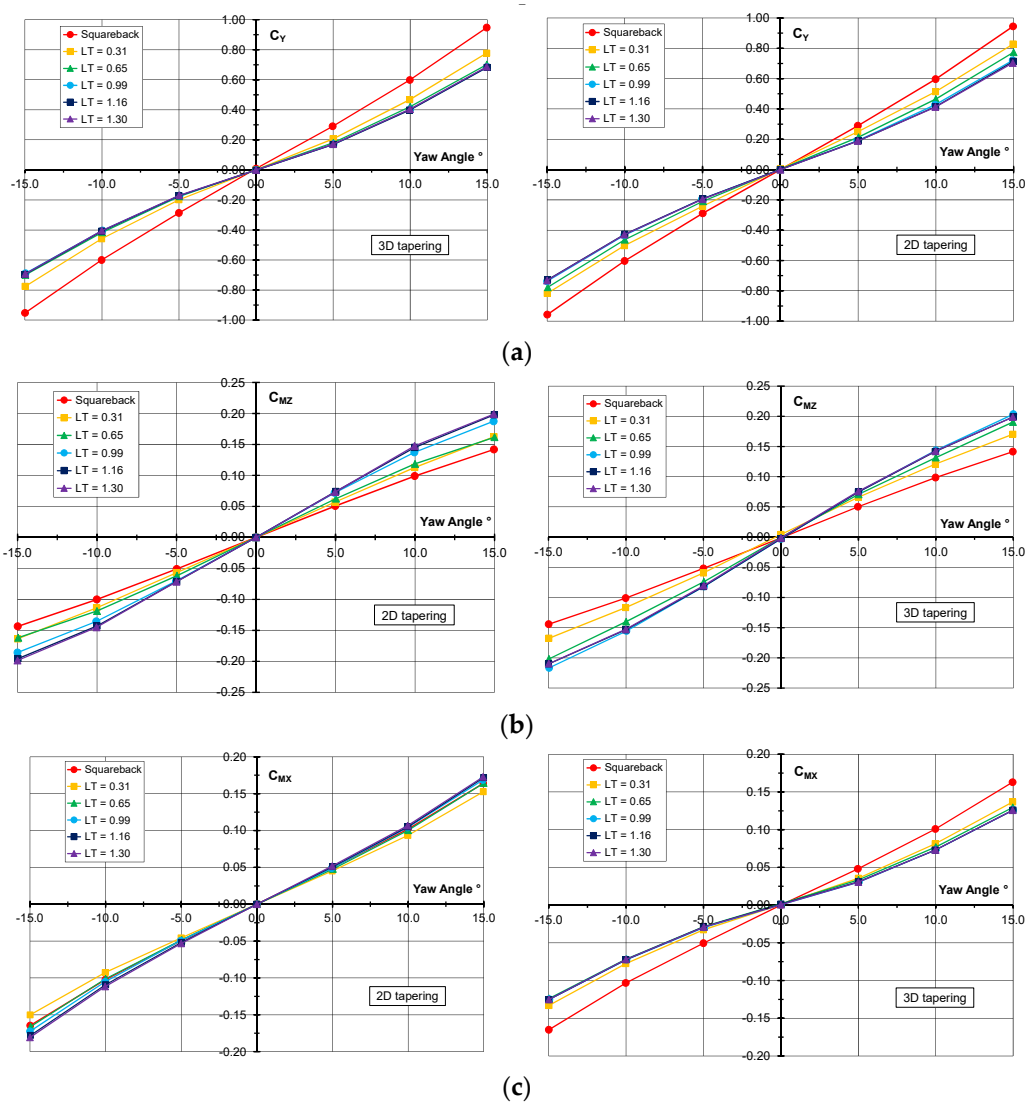


Figure 5. (**a**). Side force coefficient. (Left) 2D tapered body, (Right) 3D tapered body. (**b**). Yawing moment coefficients. (Left) 2D tapered body, (Right) 3D tapered body. (**c**). Rolling moment coefficients. (Left) 2D tapered body, (Right) 3D tapered body.

As shown in Figure 5c, the rolling moment coefficient increase at yaw for the 2D case is largely unaffected by adding the tails. For the 3D tapered bodies, the rolling moment is reduced by adding the tapered rear body, although there is no further change from increasing tail length. The rolling moment becomes non-linear with the added tails.

For all the lateral aerodynamic characteristics, the increase in non-linearity tends to produce comparable derivatives with yaw with the squareback case at larger yaw angles. Some implications of these lateral aerodynamic characteristics for crosswind sensitivity are considered in the following Discussion section.

4. Discussion

4.1. Effect of Adding Tapered Tails

The effect of adding the tapered tails on the drag and lift coefficients at zero yaw for both 2D and 3D tapered cases are shown in Figure 6, where the coefficients are plotted as a function of tail length. The significantly greater reduction in drag and reduction in the lift increase from adding the tapering of the rear body-sides to the roof slant is clearly shown.

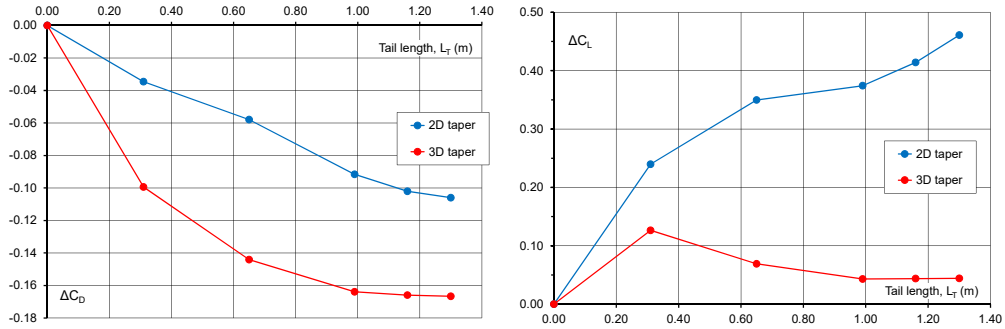


Figure 6. Drag coefficient reduction, (**left**), and lift coefficient increase, (**right**), from adding the tapered tail.

The lift and drag changes in the 2D case arise from the pressures generated on the slant and base surfaces, as shown by Howell et al. [6,7]. Figure 7, reproduced from [7], shows the pressure distribution on the slant surface of the body with a long tail. The strong suction on the side edges of the slant arise from the edge vortices. By tapering the sides of the tail as shown in Figure 7 (right), the surfaces experiencing a strong suction are removed.

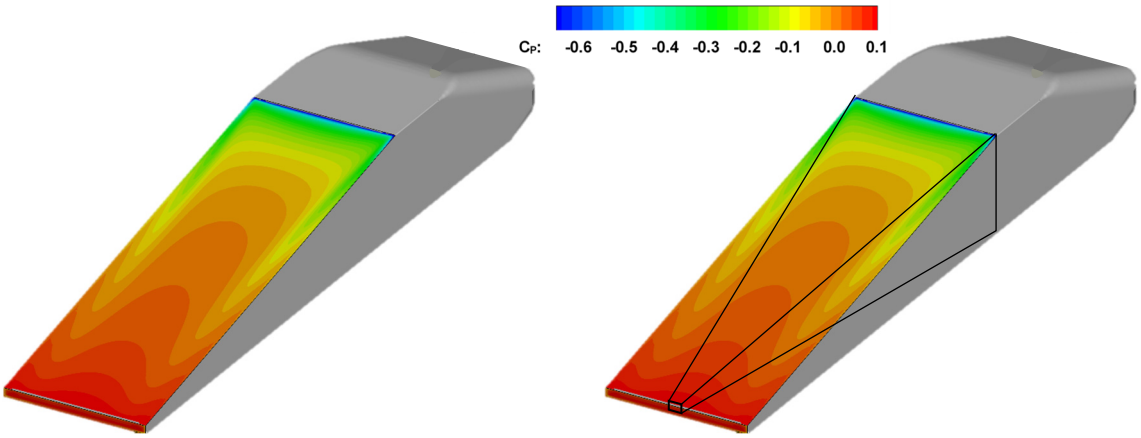


Figure 7. Pressure distribution on the slant surface of the Windsor body with a long tail, (**left**) and with the side taper geometry superimposed, (**right**).

The lift reduction for the 3D tapered tails can be ascribed mainly to the suppression of the edge vortices on the slant, although the reduced slant surface area has an effect. The resulting removal of the strong suction on the slant surface associated with these vortices also contributes strongly to the increased drag reduction combined with the reduction in base area. An additional drag component will, however, be present in the 3D case on the tapered side surfaces. The maximum drag benefit from adding the fully streamlined tail is increased by almost 60% by including tapering on the sides of the tail. At half the full length tail, the drag reduction in the 2D case is 55% of the maximum achievable, while for the 3D case it is 83%. This latter result is potentially what gave rise to the old anecdotal idea that a good compromise for drag was to chop off half the tail.

In the case of lift the increase with tail length, it is very different for the two cases. While in the 2D case it tends to increase continually with tail length, for the 3D case the initial increase in lift from introducing the slant is followed by a continual reduction in lift.

The drag data shown in Figure 6 is replotted in Figure 8 as a function of the change in base area ratio; the ratio of the base area, A_B, to the frontal area, A. Comparing Figure 8 with Figure 6, the 2D case shows the same approximately linear relationship, but for the 3D configuration the initial drag reduction is greater than the 2D case, but the difference is less pronounced. At a base area ratio of 0.5, the drag reduction for the 2D case is, as before,

55% of the maximum, while for the 3D case the reduction ratio is 66%. It can also be seen that for area ratios greater than 0.5 the trends are similar for the two cases. This trend is confirmed by considering the drag rise due to truncating the streamlined tail cases.

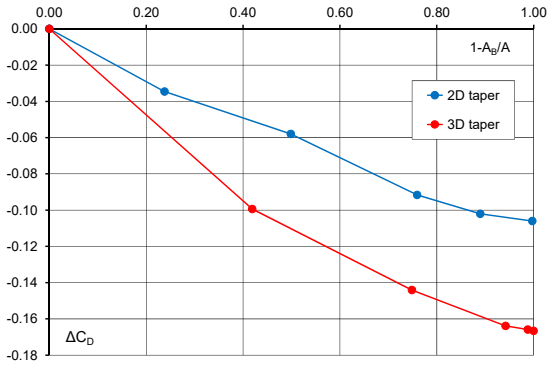


Figure 8. Drag reduction as a function of base area ratio.

Figure 9 shows the drag increase from truncating the streamlined tails for the two cases as a ratio of the drag increase at a base area ratio of 0.5. The drag increase varies with the base area ratio to the power of 1.5. This result is in agreement with the prediction of Hoehner [8] and applies to both tapered cases with base area ratios up to 0.5. Although not shown in Figure 9, the relationship is approximately true for all the tails in the 3D case.

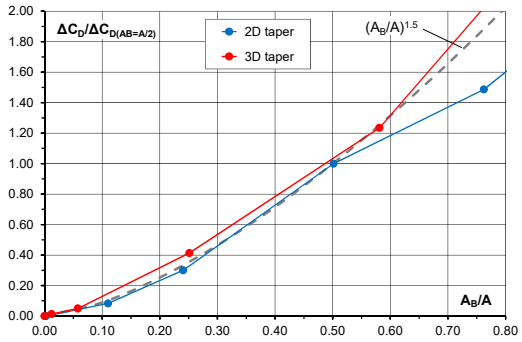


Figure 9. Drag increase from truncating streamlined tail.

4.2. Crosswind Sensitivity

A body at a yaw angle in the wind tunnel can crudely represent a body immersed in a steady crosswind. The lateral aerodynamic characteristics can influence the sensitivity of a vehicle to crosswinds. The side force variation with yaw shown in Figure 5a suggests that the side force derivative reduces as the tail length is increased. The introduction of planform tapering has little effect. The reduction of the side force at a given yaw angle for the longer bodies is noticeable, as it occurs as the side area is increasing. It is, however, consistent with other studies, such as Howell, [11], of side forces on simple bodies and cars at yaw.

While this might be considered beneficial, the yawing moment is a more important measure of crosswind sensitivity, and this shows an opposite effect, as seen in Figure 5b. The increase in yawing moment at a given yaw angle as tail length increases occurs when the side area aft of the rear axle is increasing. This increase and the forward movement of the centre of pressure with increasing tail length in part explains why low drag bodies are sometimes associated with increased crosswind sensitivity. As with side force, the planform taper has a negligible effect.

Rolling moment does not have a significant role in influencing the crosswind sensitivity of passenger cars unless they are tall and lightweight. This is the only lateral aerodynamic

characteristic which is noticeably influenced by the planform tapering. The rolling moment at a given yaw angle is reduced for the 3D taper case. Interestingly, the rolling moment is not affected by tail length.

4.3. Drag and Lift Breakdown—2D Case

In the case of the 2D streamlined tail, pressure data obtained over the rear body allows the drag and lift components from the different surfaces to be derived. The breakdown of the components contributing to the overall drag and lift are shown in Figure 10. The overall drag and lift coefficients, C_D and C_L, as measured by the wind tunnel balance, are shown by the green data. The base drag coefficient, C_{DB}, shown in red, falls sharply as the tail length increases, becoming close to zero at a tail length of 1.0 m, and remains close to zero for longer tails. The drag reduction arises from a combination of reducing base area and increasing base pressure with increasing tail length. The slant surface drag coefficient, C_{DS}, shown in blue, initially increases with tail length, becoming a maximum at half the maximum tail length, and then reduces very slightly as the tail lengthens. The latter effect occurs when there is positive pressure on the upper tail surface near the trailing edge of the longest tailed bodies, as shown in [7]. The skin friction component, C_{DSF}, shown in purple, has been obtained from the CFD simulation for these bodies, reported in [6]. The forebody drag coefficient, C_{DFB}, shown in dark blue, is then derived by subtracting the sum of these components from the overall drag coefficient;

$$C_{DFB} = C_D - (C_{DB} + C_{DS} + C_{DSF}), \quad (3)$$

and is seen to be almost constant.

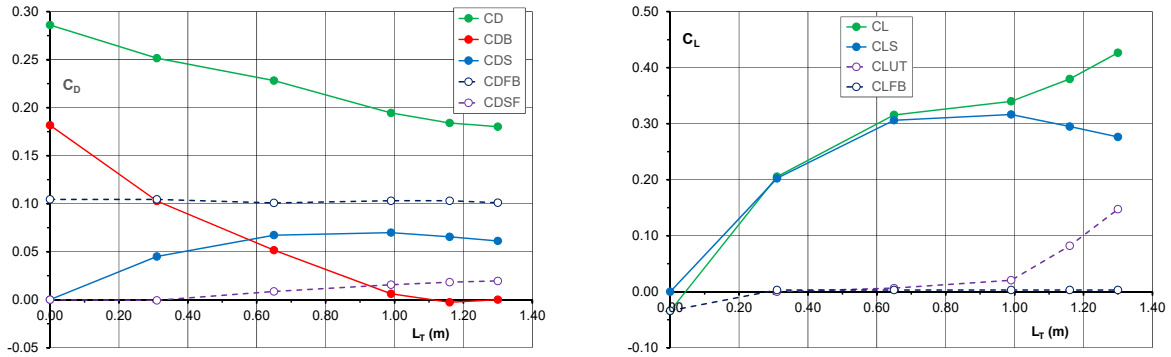


Figure 10. Breakdown of drag, (**left**), and lift, (**right**), coefficients for 2D taper case.

For the breakdown of lift, the slant surface lift coefficient, C_{LS}, shown in blue, follows the overall lift coefficient trend closely up to a tail length of 1.0 m, after which it reduces slightly while the overall lift increases. The difference between the slant surface and the overall lift coefficient for tail lengths longer than 0.31 m represents the incremental lift coefficient on the underside of the tail, C_{LUT}, and is shown in purple. This also assumes that the forebody lift coefficient, C_{LFB}, shown in dark blue, is constant, for these tails, where the forebody includes all upper surfaces forward of the leading edge of the slant surface and the underbody surface back to the trailing edge of the underfloor of the squareback (and initial slant surface) body. The squareback body includes the additional upper surface aft of the slant leading edge position. The increase in tail underfloor lift coefficient with the longest tails arises from the positive pressure in this region and the build-up of the boundary layer on the underside of the tail and ground surfaces.

A crude theory to predict the lift behaviour on the slant surface is provided in Appendix A. This suggests that the lift is enhanced by the action of the edge vortices, similar to the effect of wing endplates. The vortex intensity is not continuously reinforced, however, but the incremental effects diminish over the length of the tail. While this is a plausible explanation, alternative suggestions include the separation of the edge vortices, similar to that occurring

on long slender bodies such as trains or missiles, and decaying vortex intensity, which arises from a transfer of the rotational energy to a longitudinal component as occurs in wake flows.

4.4. Base Pressure

The mean base pressure coefficient obtained for the 2D tapered case is shown in Figure 11, as a function of the base area ratio. Also shown is the base pressure coefficient for the same body fitted with wheels as reported in [7].

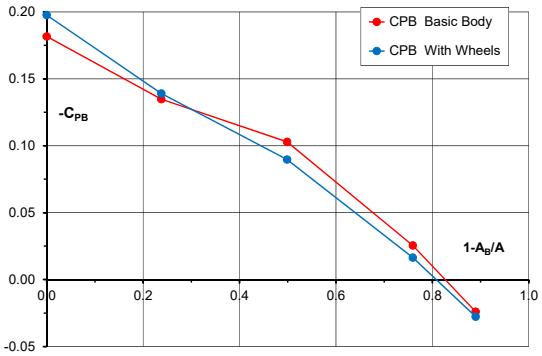


Figure 11. Base pressure coefficient for 2D taper case, with and without wheels.

The trends are similar for both cases with the base pressure coefficient increasing markedly as the base area reduces. The base pressure coefficient becomes positive, generating a small thrust when the base area is approximately 20% of the body cross section area. The base pressure coefficients for the squareback Windsor model with and without wheels was previously measured by Varney, [12]. While for his model without wheels the base pressure coefficient was very similar, $C_{PB} = -0.177$ (c.f. -0.182), the base pressure increase from adding wheels was only 4%, compared to an increase of 9%, as shown here.

4.5. D Tapering

No pressure data was obtained on the rear end surfaces of the Windsor body with tapering on the upper rear and side surfaces. A breakdown of the drag and lift components is not, therefore, directly available, but some observations can be made based on the forces measured.

The base drag coefficient will reduce more rapidly with tail length because the base area reduction is greater. Assuming that the base pressure coefficient will increase with reducing the base area ratio as shown in Figure 11, this drag reduction will be enhanced.

On the slant surface the initial suction close to the slant leading edge will be comparable to that for the 2D case, producing lift and a trailing vortex. This vortex will not, however, be reinforced by edge vortices, and the strong suction on the side edges of the upper slant surface will not exist. At the same time, the pressure recovery on the slant will be greater than for the 2D situation and the slant surface area is reduced with the side tapers. These effects result in a substantially lower slant surface drag component.

There will be an additional drag component on the tapered side surfaces. A suction can be expected on the side taper leading edge similar to that on the slant surface, albeit lower because the taper angle is less. Any pressure recovery on the side taper will be less than on the slant and the total area is greater. The side taper drag component is unknown, but will be small. The forebody drag will effectively be the same as in the 2D case, but the total drag for the 3D configuration will reduce significantly more with increasing tail length than in the 2D case.

The Lift on the forebody will be approximately the same for both the 2D and 3D tapered cases. On the upper slant surface the initial suction near the leading edge will be comparable, but the pressure recovery along the slant, the absence of suction beneath the

edge vortices and the reducing body width will result in much lower lift on the slant of the body with side tapers. There is no lift generated on the side tapered surfaces or the base. On the underbody of the tail, the lift produced is reduced because the planform surface area is much smaller. The net result of these changes as shown by the total lift variation in Figure 5 with a strong reduction in lift with increasing tail length following an initial lift increase is difficult to explain without any pressure or flow visualisation data.

Using the assumptions above, the suggested breakdown of the overall lift and drag coefficients is shown in Figure 12. In the lift case, Figure 12 (right), the lift on the underside of the tail, C_{LUT}, is assumed to vary with the reduced surface area while the forebody lift coefficient is unchanged from the 2D case. The slant surface lift, C_{LS}, is then simply the total lift, C_L, less C_{LUT}. Note the significant change of the lift coefficient scale in comparison with Figure 10.

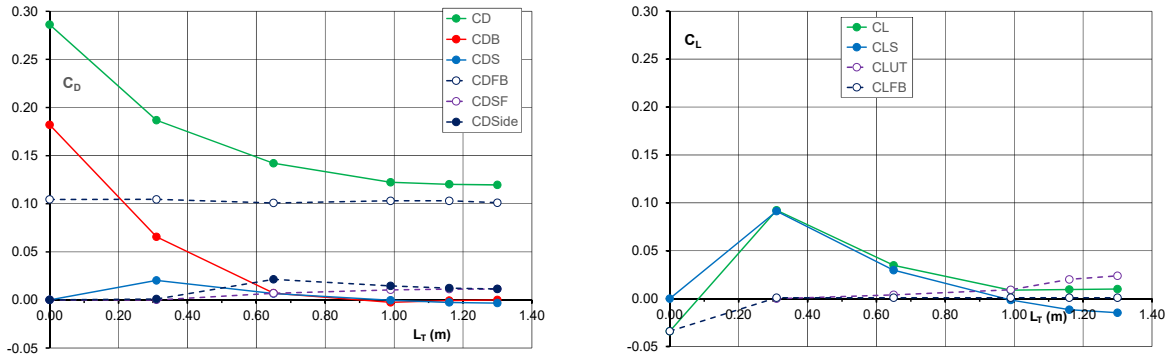


Figure 12. Suggested breakdown of drag, (**left**), and lift, (**right**), coefficients for 3D taper case.

For the drag breakdown, Figure 12 (left), the slant surface drag coefficient, C_{DS}, is derived directly from the slant surface lift. The base pressure coefficient is assumed to vary as shown in Figure 11, based on the base area ratio, and the base drag coefficient, C_{DB}, is then the product of base pressure coefficient and base area. The skin friction drag coefficient, C_{DSF}, is modified based on the change in surface area and the forebody drag is assumed to be the same as the 2D case. The remaining drag component on the tapered side surfaces, C_{DSide}, is then given by the difference between the total drag coefficient, C_D, and the sum of the base, slant, forebody and skin friction components.

4.6. Final Comments

It should be noted that the authors are not advocating long streamlined tails as a means of achieving significant drag reductions, but these are a consequence of a systematic evolution of the tapered state and provide some insight into the flow mechanisms that exist on highly tapered configurations.

The potential for further drag reduction from optimisation of the taper angles and by adding an underbody diffuser and/or a base cavity should be assessed in future testing.

5. Conclusions

A wind tunnel experiment has been conducted on the Windsor body with a streamlined tail of variable length tapered on the upper and side surfaces, identified in this paper as the 3D case. The results have been compared with the tail tapered on the upper body only, here called the 2D case.

Drag and lift coefficients at zero yaw are substantially reduced from the addition of planform tapering because the edge vortices on the slant surface are suppressed. The increase in both drag and lift coefficients at yaw are also considerably reduced.

The lateral aerodynamic characteristics, side force and yawing moment, are effectively unchanged for the 3D case in comparison with the 2D body at a given yaw angle. Only the rolling moment shows a reduction.

The maximum drag coefficient reduction from adding a fully streamlined tail, with tapering on the top and sides, to the squareback body is $\Delta C_D = -0.167$, which is almost 60% greater than for the 2D case.

The reduction of overall drag with tail length and with base area ratio is considerably greater for the 3D tail than for the 2D case.

Lift initially increases with tail length for the 3D configuration but then decreases for all of the tested tails, while for the 2D case the lift is increased with increasing tail length, except for the very longest tails.

The breakdown of drag with tail length is deduced for the 3D tapered case and compared with the measured values for the 2D configuration. For a given tail length the drag on the slant surface of the 3D tail is reduced due to the lower vortex drag and the base drag component is reduced because the base area is smaller and the base pressure is higher, but this is offset by a drag component from the tapered side surfaces.

The increase in the drag coefficient from truncating the streamlined tail varies with the base area ratio to the power of 1.5.

Author Contributions: J.H.: data analysis, writing draft and final paper; M.V., model design, wind tunnel testing; D.B., paper review & editing; M.P., conceptualization, authorization. All authors have read and agreed to the published version of the manuscript.

Funding: This research received no external funding.

Data Availability Statement: The data can be available on request to the corresponding author.

Acknowledgments: The authors are grateful to Andy Horsey for building the model tails. Max Varney, who designed the model tails for the Windsor Body, conducted all the wind tunnel testing and collated the data, is now at Mercedes F1.

Conflicts of Interest: The authors declare no conflict of interest.

Appendix A. A Theory for Lift on a 2D Streamlined Tail

The variation of slant surface lift with tail length as demonstrated in Figure 8 shows an initial linear increase which then levels off. A maximum lift is achieved at a tail length of approximately 60% of the fully streamlined case, followed by a small reduction. In an attempt to explain this behaviour, consider the effect of aspect ratio on lift. For wings, the effect of aspect ratio on the slope of the lift coefficient, $C_L{}'$, with incidence, α, is usually approximated by:

$$C_L{}'/\alpha = 2\pi/(1 + A_R/2) \quad \text{(A1)}$$

where A_R is the aspect ratio of the wing, and is given by w^2/A', where w is the wing span and A' is the wing area. For low aspect ratios in the range 0.5 to 5, which is of more relevance to the car shapes, a more accurate representation is given by:

$$C_L{}'/\alpha = 2\pi/(1 + A_R/3), \quad \text{(A2)}$$

which gives the slope as 2π for a 2D wing of infinite aspect ratio and equals $\pi/2A_R$ at very low aspect ratios, as given by slender wing theory. For a wing the coefficient is based on the wing area. In the case of the car-like body considered here, the coefficients are based on the frontal area, A. The backlight/slant surface is the equivalent of the upper wing surface, and the lift coefficient, C_L, for a slant angle, φ, becomes:

$$C_L/\varphi = \pi A_S/(A(1 + A_R/3)), \quad \text{(A3)}$$

where A_S is the area of the slant surface. The action of the edge vortices on the slant surface acts like an endplate at the wing tip according to Küchemann [13]. For a slender wing with endplates, the lift coefficient is increased by a factor (1 + h/s), [N], where h is the height of the endplate at the wing trailing edge and s is the wingspan. In the case of a rectangular

backlight on a car-like shape such as the Windsor body, the lift coefficient, as a function of L_S the slant length, becomes:

$$C_L/\varphi = \pi L_S W\,(1 + h/W)/(H(W + 3L_S)). \quad (A4)$$

For an approximation of the height, h, consider Figure A1. If the flow along the bodyside, just upstream of the slant surface, is aligned with the freestream with velocity U, the flow velocity normal to the slant surface, with slant angle, φ, outside the separating shear layer, is $U\varphi$. Inside the shear layer, the velocity is zero. The shear layer, therefore. grows with a velocity $U\varphi/2$. If these conditions are maintained all along the slant edge, the shear layer height above the slant surface, at the trailing edge, is simply $\varphi L_S/2$.

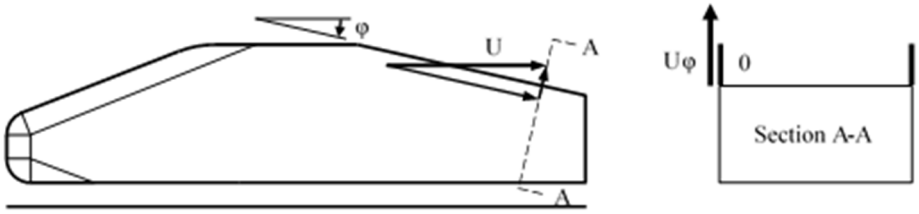


Figure A1. Slant edge flow schematic.

In reality, the flow streamline approaching the slant edge varies along the slant length and becomes increasingly aligned with the slant edge towards the base of the body in part because of the significant pressure recovery along the slant surface. The flow velocity outside the separating shear layer therefore reduces along the slant length and can be represented by $U\alpha$ where α is a function of φ and L. The height of the shear layer, h, at the trailing edge of the slant is then given by:

$$h = \int_0^L \alpha/2\; dl_T \quad (A5)$$

where l_T denotes the length along the slant

There is an increasing pressure gradient on the slant which is approximately linear over most of the length, as shown in [7]. At the leading edge the surface pressure can be considered to be proportional with the slant angle, φ. The surface pressure on the side of the tail is approximately constant along the length of the tail and is slightly negative. It is assumed that the angle α is related to the pressure difference between the body side and the slant surface, and also that the pressure gradient is proportional to φ^2. The latter relationship is because the slant pressure coefficient increases to a value close to zero at the trailing edge of the fully streamlined tail, so the pressure increase over the tail length is proportional to φ and the tail length is approximately proportional to φ. The angle, α, and the shear layer height, h, are then given by:

$$\alpha = k_2\varphi - k_3\varphi^2\,(l_T/H) \quad (A6)$$

$$h = k_2\varphi L_S/2 - k_3\varphi^2 {L_S}^2/4H \quad (A7)$$

If Equation (A4) is written as $C_L/\varphi = (C_L/\varphi)_0\,(1 + h/W)$, then:

$$C_L/\varphi = (C_L/\varphi)_0\,(k_1 + L_S\varphi/2W(k_2 - k_3 L_S\varphi/2H) \quad (A8)$$

where k_1 is introduced to account for the lift that occurs on the roof of the body upstream of the slant leading edge. This factor will be slightly greater than 1.0 but can be assumed to be proportional to the lift on the slant, especially for lower slant lengths. The lift coefficient increase due to the slant as a function of slant length for a slant angle of 12.5° is plotted in Figure A2 and compared with the experimental lift data from Figure 8. In Figure A2 the incremental lift data is the lift increase relative to the squareback case less the increase in lift from the underside of the tail. Also included in Figure A2 is the experimental data for

lower slant aspect ratio backlights on the Windsor Body as presented in Howell et al. [7], from the data of Howell and Le Good [14] and Pavia, [15]. In the latter cases, the lift data is interpolated to provide the lift coefficients for a slant angle of 12.5°.

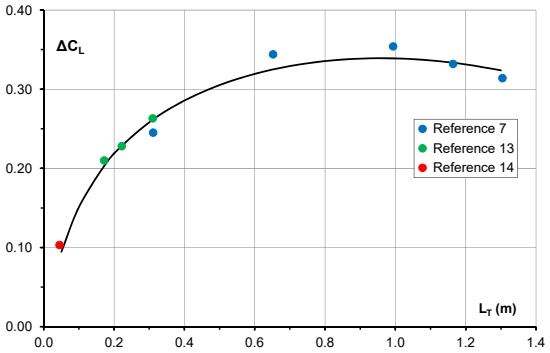


Figure A2. Lift increase as a function of slant length.

The theoretical lift curve is achieved using constants $k_1 = 1.08$, $k_2 = 1.70$, and $k_3 = 1.80$, and provides a reasonable qualitative fit to the experimental data. It may be noted that the lift Equation (A8) generates a non-linear increase of lift with a slant angle for a given tail length of the form:

$$C_L = A\varphi + B\varphi^2 - C\varphi^3 \quad \text{(A9)}$$

The experimental data for low aspect ratio slant surfaces suggests that lift variation with slant angle is linear (see Howell and Le Good, [13]), but comparing this data with the theoretical curves as shown in Figure A3 indicates that the non-linearity is not pronounced, in part because the positive second order effects are offset by the negative third order effects.

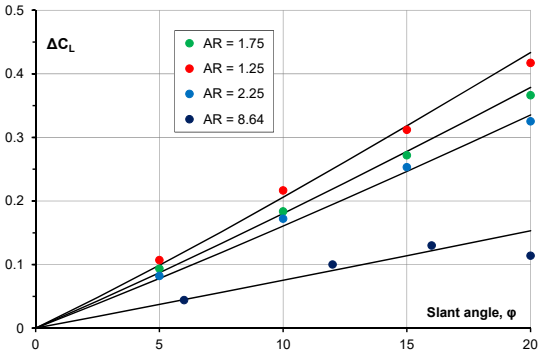


Figure A3. Lift increase as a function of slant angle.

References

1. Ludvigsen, K. *The Time Tunnel–An Historical Survey of Automobile Aerodynamics*; Technical Paper 700035; SAE: Warrendale, PA, USA, 1 February 1970. [CrossRef]
2. Koenig-Fachsenfeld, R.V. *Aerodynamik des Kraftfahrzeuges*; Umschau Verlag: Frankfurt, Germany, 1951.
3. Hucho, W.-H. (Ed.) *Aerodynamics of Road Vehicles*, 4th ed.; SAE R-177; SAE International: Warrendale, PA, USA, 1998; ISBN 0-7680-0029-7.
4. Schütz, T. (Ed.) *Aerodynamics of Road Vehicles*, 5th ed.; SAE R-430; SAE International: Warrendale, PA, USA, 2016; ISBN 978-0-7680-7977-7. [CrossRef]
5. Edgar, J. *A Century of Car Aerodynamics*; Amazon, Independently published: London, UK, 2021; ISBN 13 979-8506846901.
6. Howell, J.; Rajaratnam, E.; Passmore, M. *Streamlined Tails–The Effect of Truncation on Aerodynamic Drag*; Technical Paper 2020-01-0673; SAE: Warrendale, PA, USA, 14 April 2020. [CrossRef]
7. Howell, J.; Varney, M.; Rajaratnam, E.; Passmore, M. *A Wind Tunnel Study of the Windsor Body with a Streamlined Tail*; Technical Paper 2021-01-0954; SAE: Warrendale, PA, USA, 6 April 2021. [CrossRef]
8. Hoerner, S.F. *Fluid Dynamic Drag*; Published by the author: Midland Park, NJ, USA, 1958.
9. Mair, W.A. Reduction of Base Drag by Boat-Tailed Afterbodies in Low-Speed Flow. *Aeronaut. Q.* **1969**, *20*, 307–320. [CrossRef]

10. Johl, G.; Passmore, M.; Render, P. Design Methodology and Performance of an In-Draft Wind Tunnel. *Aeronaut. J.* **2004**, *108*, 465–473. [CrossRef]
11. Howell, J.; Panigrahi, S. *Aerodynamic Side Forces on Passenger Cars at Yaw*; Technical Paper 2016-01-1620; SAE: Warrendale, PA, USA, 5 April 2016. [CrossRef]
12. Varney, M. Base Drag Reduction for Squareback Road Vehicles. Ph.D. Thesis, Loughborough University, Loughborough, UK, 2019.
13. Küchemann, D. *The Aerodynamic Design of Aircraft*; Pergamom Press: Oxford, UK, 1978; ISBN 0-08-020515-1.
14. Howell, J.; Le Good, G. *The Effect of Backlight Aspect Ratio on Vortex and Base Drag for a Simple Car-like Shape*; Technical Paper 2008-01-0737; SAE: Warrendale, PA, USA, 14 April 2008. [CrossRef]
15. Pavia, G. Characterisation of the Unsteady Wake of a Square-Back Vehicle. Ph.D. Thesis, Loughborough University, Loughborough, UK, 2019.

Disclaimer/Publisher's Note: The statements, opinions and data contained in all publications are solely those of the individual author(s) and contributor(s) and not of MDPI and/or the editor(s). MDPI and/or the editor(s) disclaim responsibility for any injury to people or property resulting from any ideas, methods, instructions or products referred to in the content.